

The Hubble constant from eight time-delay galaxy lenses

Philipp Denzel,^{1,2} * Jonathan P. Coles,³ Prasenjit Saha,^{2,1} Liliya L. R. Williams⁴

¹*Institute for Computational Science, University of Zurich, 8057 Zurich, Switzerland*

²*Physics Institute, University of Zurich, 8057 Zurich, Switzerland*

³*Physik-Department T38, Technische Universität München, James-Frank-Str. 1, D-85748 Garching, Germany*

⁴*School of Physics and Astronomy, University of Minnesota, 116 Church Street SE, Minneapolis, MN 55455, USA*

ABSTRACT

We present a determination of the Hubble constant from the joint, free-form analysis of 8 strongly, quadruply lensing systems. In the concordance cosmology, we find $H_0 = 71.8^{+3.9}_{-3.3} \text{ km s}^{-1} \text{ Mpc}^{-1}$ with a precision of 4.97%. This is in agreement with the latest measurements from Supernovae Type Ia and Planck observations of the cosmic microwave background. Our precision is lower compared to these and other recent time-delay cosmography determinations, because our modelling strategies reflect the systematic uncertainties of lensing degeneracies. We furthermore are able to find reasonable lensed image reconstructions by constraining to either value of H_0 from local and early Universe measurements. This leads us to conclude that current lensing constraints on H_0 are not strong enough to break the “Hubble tension” problem of cosmology.

Key words: Gravitational lensing: strong, cosmological parameters

1 INTRODUCTION

In the flat Λ -cold dark matter model of cosmology (Λ CDM), the rate at which the Universe expands on large scales is

$$\frac{da}{dt} = H_0 \left(\frac{\Omega_m}{a} + \frac{\Omega_r}{a^2} + \Omega_\Lambda a^2 \right)^{1/2} \quad (1)$$

where a is the scale factor and t is the cosmic time. The Hubble constant H_0 is defined as the \dot{a}/a at the current epoch and sets the overall scale. The fractional contribution of the non-relativistic and relativistic mass-energy and dark energy components is captured by the $\Omega_i = \rho_i/\rho_c$ parameters, which are normalized by

$$\rho_c = \frac{3H_0^2}{8\pi G} \quad (2)$$

the cosmological critical density. Local variations (galaxies) around the mean density arise from an initial fluctuation spectrum described by further cosmological parameters. This model (for a ‘skeptical’s guide’ see [Scott 2018](#)) succeeds in describing a multitude of phenomena including the accelerating rate of expansion, the statistics of fluctuations both in the local Universe and in the cosmic microwave background (CMB), and the abundances of the light elements. Yet despite an increasing number of successes with measurements of unprecedented precision, some unsolved puzzles remain. Among these is the tension in the values of H_0 from standard candles (in particular, $74.0 \pm 1.4 \text{ km s}^{-1} \text{ Mpc}^{-1}$

from the SH0ES (Supernovae H_0 for the Equation of State) project by [Riess et al. 2019](#)) and from the CMB (most recently $67.4 \pm 0.5 \text{ km s}^{-1} \text{ Mpc}^{-1}$ from the Planck collaboration [Aghanim et al. 2018](#)).

These measurements (sometimes called ‘late’ and ‘early’) represent two fundamentally different strategies for measuring cosmological parameters, and involve completely different physical processes. The first of these involves a redshift-distance relation, whereby one measures how the comoving distance

$$r(a) = c \int \frac{dt}{a(t)} \quad (3)$$

(or some variant of it) depends on redshift $z = 1/a - 1$. Standard-candle methods, gravitational-lensing time delays, and anticipated methods using gravitational-wave sources all use redshift-distance relations. In contrast, measurements of cosmological parameters from the CMB or from baryon acoustic oscillations use a different strategy, where the main observable is the angular power spectrum on the sky of acoustic oscillations in the Universe from epochs when structure growth was linear. The angular scale of the largest features is set by the apparent size of the horizon $\theta_h(a)$ at the relevant redshift where

$$\theta_h^{-1}(a) = \frac{r(0)}{r(a)} - 1. \quad (4)$$

There is no explicit redshift-distance relation involved. Instead, H_0 is inferred through the effect of the component densities $\propto H_0^2/G$ on the acoustic oscillations. Comparing the H_0 values from these completely different physical pro-

* Email: phdenzel@physik.uzh.ch

cesses is an important test of the Λ CDM paradigm. If the ‘Hubble tension’ is confirmed as a discrepancy, many alternative cosmological theories will need to be considered (see e.g. Knox & Millea 2020).

For the redshift-distance relation, thermonuclear supernovae (SNeIa) as standard candles have been the leading method for some time (Sandage et al. 2006; Freedman et al. 2012; Riess et al. 2016, 2018, 2019). The uncertainty in this technique is mainly that the intrinsic brightness of SNeIa is difficult to determine, and requires a ‘distance ladder’ for calibration from other distance measurements in the local Universe (Pietrzyński et al. 2019; Reid et al. 2019; Freedman et al. 2019). Distance measurement using gravitational waves has only recently become feasible (Abbott et al. 2017) and is especially interesting because no separate calibration is required. The period and period derivative (chirp) of a gravitational-wave binary give $1+z$ times the orbital energy of the binary. The two gravitational-wave polarisations have amplitudes of orbital energy divided by distance times inclination-dependent factors. If both polarisations are measured, inclination and distance both get measured. From acoustic oscillations, the CMB results from Planck (Aghanim et al. 2018) and earlier from WMAP (Wilkinson Microwave Anisotropy Probe; Hinshaw et al. 2013) are the best known, but there are also several measurements of cosmological parameters using a combination of galaxy clustering, weak lensing, baryonic acoustic oscillations, and primordial nucleosynthesis (Abbott et al. 2018a,b; Alsing et al. 2016; Hildebrandt et al. 2016; Anderson et al. 2012).

Gravitational-lensing time delays present another form of redshift-distance relation, involving multiple distances within one system. As lensing time delays are the subject of the present paper, we introduce the basic equation here, in the variational formulation following Blandford & Narayan (1986) with small changes of notation. Consider a virtual light ray originating at a source at β on the sky, and at distance D_S from the observer. In front of the source, at redshift z_L and distance D_L from the observer, lies a gravitational lens consisting of a thin mass distribution $\Sigma(\theta)$. The virtual ray gets deflected at the lens and reaches the observer from θ on the sky. The arrival-time surface $t(\theta)$ of this virtual light ray is

$$\frac{t(\theta)}{(1+z_L)} = \frac{D_L D_S}{2c D_{LS}} (\theta - \beta)^2 - \frac{8\pi G}{c^3} \nabla^{-2} \Sigma(\theta) \quad (5)$$

where D_{LS} is the distance from the lens to the source. Although these are all angular-diameter distances, and hence $D_{LS} \neq D_S - D_L$, the distances are still strictly proportional to c/H_0 . That is, H_0^{-1} sets the scale of Eq. (5). Real light rays correspond to $\nabla t(\theta) = 0$, namely minima, saddle points, and maxima of $t(\theta)$, and these are the locations of multiple images. If the source varies in time, the differences (or time delays) between $t(\theta_i)$ at multiple images can be measured. For variable sources such as quasars the differences in arrival times are usually of the order several days to a year, but if the lens systems are highly symmetric or have merging triplets, their delays can be well under an hour. With accurate measurements of the time delays, it is possible to determine a time scale which is proportional to H_0^{-1} . This makes strong gravitational lenses excellent cosmological probes because they enable a determination of H_0 completely independent of the cosmic distance ladder. Lensing time delays have therefore

been the subject of many observational campaigns, the most recent results reported in Millon et al. (2020a) and Millon et al. (2020b).

The early theoretical work (Refsdal 1964; Refsdal 1966) considered point-like sources and lenses. But as soon as lenses were discovered, it became clear that extended mass distributions $\Sigma(\theta)$ and extended sources would need modelling. The resulting model-dependence of inferences was noted already in the first paper modelling lensing data (Young et al. 1980) and has been explored in many later works (e.g. Saha & Williams 2006; Schneider & Sluse 2014; Wagner 2018; Denzel et al. 2020). If there are many lensed sources at different redshifts, each lensed into multiple images, $\Sigma(\theta)$ will be well constrained by them. Ghosh et al. (2020) estimate that if there are 1000 lensed images, a single precise time-delay measurement would measure H_0 to sub-percent accuracy, and that this may be feasible with JWST observations of cluster lenses. Galaxy lenses, however, rarely have more than one source lensed into four images, so the best strategy is to combine many lenses. That said, multiple-source lens systems such as the ‘jackpot’ double Einstein ring, for which just recently a third source has been reported by Collett & Smith (2020), have been found to reduce degeneracies substantially and should therefore reduce uncertainties on H_0 inferences (Gavazzi et al. 2008) if time-delay measurements in such systems become available. Sereno & Paraficz (2014) report a 10% uncertainty on H_0 using 18 time-delay lenses. Smaller uncertainties on H_0 are possible—2.5% from six lenses by the H0LiCOW collaboration (H_0 Lenses in COSMOGRAIL’s Wellspring; Wong et al. 2020) and 4% uncertainty from a single lens (Shajib et al. 2020)—if it is assumed that galaxy lenses follow certain parametric forms. Gilman et al. (2020) demonstrate using mock observations based on real lens configurations that perturbations from substructure contribute an additional source of random uncertainty in the inferred value of H_0 . If these substructures are fitted properly, they could to a certain degree improve cosmographic inferences from single galaxy lenses. Uncertainties on H_0 increase however if lensing degeneracies are considered, but may be alleviated again if stellar kinematics are considered, e.g. (Birrer et al. 2020). In a recent blind test involving several research groups, the Time Delay Lens Modelling Challenge (TDLMC; Ding et al. 2020), the currently achievable error level in the recovery of simulated H_0 from up to 16 lenses was found to be 6%.

The Hubble constant is commonly expressed in units of $\text{km s}^{-1} \text{Mpc}^{-1}$. This choice reflects Hubble’s law by stating that the Hubble constant is the recession speed of a target galaxy over its distance. However, it is arguably more natural to think of the Hubble constant as a reciprocal time or frequency. Of course, the Hubble time H_0^{-1} is already in units of Gyr and proportional to the age of the Universe. In the current epoch, the Hubble parameter seems to be close to steady and consequently, distances scale (nearly) exponentially with $a \propto e^{Ht}$ due to the increasingly dominant dark-energy density component. In this context, it is interesting to express the Hubble constant in SI units as *attohertz* ($\text{aHz} = 10^{-18} \text{s}^{-1}$). Since the Hubble tension has been a persistent problem, a change of units also provides a new perspective on the issue and might promote new ideas. One should recall that the

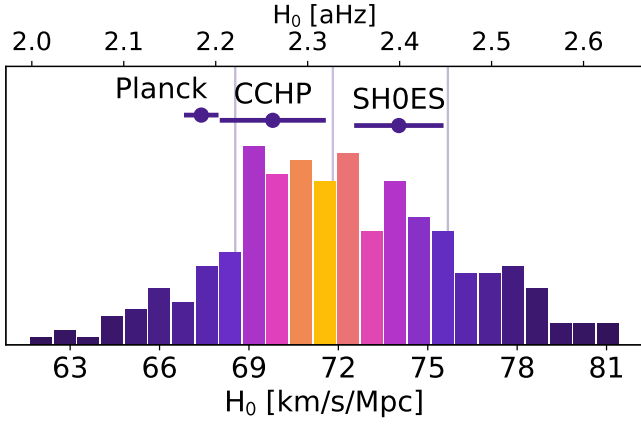


Figure 1. The main result: an ensemble of H_0 values inferred from the joint modelling of eight four-image time-delay lenses. Vertical lines indicate the median 68 per-cent confidence range of $H_0 = 2.33^{+0.13}_{-0.11}$ aHz = $71.8^{+3.9}_{-3.3}$ km s⁻¹ Mpc⁻¹. To make the median furthermore easily discernible, the colouring of the histogram’s bars corresponds to the cumulative probability centred around the median (yellow-magenta-blue-black goes from 1 to 0). Horizontal error bars indicate recent measurements from other methods for comparison: Planck (Aghanim et al. 2018), CCHP (the Carnegie-Chicago Hubble Program; Freedman et al. 2019), and SH0ES (the Supernovae H_0 for the Equation of State; Riess et al. 2019). A discussion of units can be found in the introduction.

following are all equivalent:

$$\begin{aligned} H_0 &= 70.0 \text{ km s}^{-1} \text{ Mpc}^{-1} = 2.27 \text{ aHz} \\ H_0^{-1} &= 14.0 \text{ Gyr} \\ \frac{3}{8\pi G} H_0^2 &= 5.16 \text{ GeV m}^{-3} \end{aligned}$$

These new units of attohertz then convey that large-scale structures undergo e-foldings with a frequency of roughly 2.3 aHz. We can compare this current day value to that of the very early Universe where 60 e-folds may have occurred in ~ 1 s (Allahverdi et al. 2020).

In this paper, we infer H_0 from 8 free-form time-delay lenses using the most recent observational data available and more flexible modelling methods. Additionally, we explore the effect of lensing degeneracies on H_0 , which is the inherent limitation to all lensing observables (Saha 2000). We demonstrate that due to these degeneracies it is possible to find solutions which fit values of H_0 measured through early and late-Universe probes. Our main findings are summarized in Figure 1.

In Section 2 below, we describe the eight lenses used in this work: B1608+656, DESJ0408-5354, HE0435-1223, PG1115+080, RXJ0911+0551, RXJ1131-1231, SDSSJ1004+4112, and WFIJ2033-4723. For each system we give an account of the research history, a short description of the image configuration and point out any other special features. Next, in Section 3, we describe the numerical techniques and methods employed to analyse the lenses and determine H_0 . We list precisely what information was used to model and constrain the lens reconstructions. Here, Subsection 3.4 describes the TDLMC in which our lens-modelling methods have been initially tested for the purpose of inferring H_0 . In Section 4, we present the detailed results of our work, namely the lens models, and derived quantities

such as radially-averaged enclosed mass profiles, time-arrival surfaces, synthetic images, and posterior distributions of H_0 , and moreover of the Hubble time and critical density. Relevant results from the TDLMC are discussed at the end of Subsection 4.4. Finally in Section 5, we summarize the main findings and discuss possible implications.

2 THE LENS SYSTEMS

The light travel time of the individual images differ if strongly lensed systems lie at cosmological distances. However, measuring time delays is a very time-consuming process and only a handful of systems are currently known with comparatively precise and robust values, meaning if multiple independent monitorings have been performed, they concur within their error margins. Due to computational constraints and their strong presence in the literature, we limited our analysis to the following 8 quadruply imaging lenses shown in Figure 2. In this section, we briefly describe the lenses and note the time delays with the image ordering provided in the respective literature.

2.1 B1608+656

This system was discovered during the first phase of the Cosmic Lens All-Sky Survey (CLASS). The system contains two lensing galaxies and clearly shows four quasar images on radio wavelengths, whereas its Einstein ring is better visible in the optical spectrum. Further data collection yielded redshifts for the lens $z_1 = 0.630$, the source $z_s = 1.394$, and hints that the lens consists of two merging galaxies (Myers et al. 1995; Fassnacht et al. 1996). After multiple seasons of monitoring (Fassnacht et al. 1999b; Fassnacht et al. 1999a; Fassnacht et al. 2002) and several robustness tests (Eulaers & Magain 2011; Holanda 2016) time delay measurements converged to $\Delta t_{AB} = 31.5^{+2.0}_{-1.0}$, $\Delta t_{CB} = 36.0^{+1.5}_{-1.5}$, and $\Delta t_{DB} = 77.0^{+2.0}_{-1.0}$ days with arrival-time order BACD. Since its discovery, many lens modellers have used the system for a determination of H_0 (Koopmans & Fassnacht 1999; Williams & Saha 2000; Koopmans et al. 2003; Fassnacht et al. 2004; Suyu et al. 2010; Wong et al. 2020).

2.2 DESJ0408-5354

This system was found and confirmed only recently in the Dark Energy Survey (DES) Year 1 (Y1) data. Subsequent spectroscopic observations using the Gemini South telescope confirmed a quasar in the source with redshift $z_s = 2.375$, and the central lens as an early-type galaxy with redshift $z_1 = 0.597$ (Lin et al. 2017). Simultaneously, high-cadence photometric monitoring results by (Courbin et al. 2018) report time-delays measurements of $\Delta t_{AB} = -112.1^{+2.1}_{-2.1}$, $\Delta t_{AD} = -155.5^{+12.8}_{-12.8}$, and $\Delta t_{BD} = 42.4^{+17.6}_{-17.6}$ days with arrival-time order ABCD. Follow-up investigations revealed the presence of a second set of multiple images at different redshifts (Agnello et al. 2017), which places it amongst the richest discoveries of lenses so far. In depth analysis of this system by the STRong-lensing Insights into Dark Energy Survey collaboration (STRIDES; Treu et al. 2018) determined $H_0 = 74.2^{+2.7}_{-3.0}$ (Shajib et al. 2020).

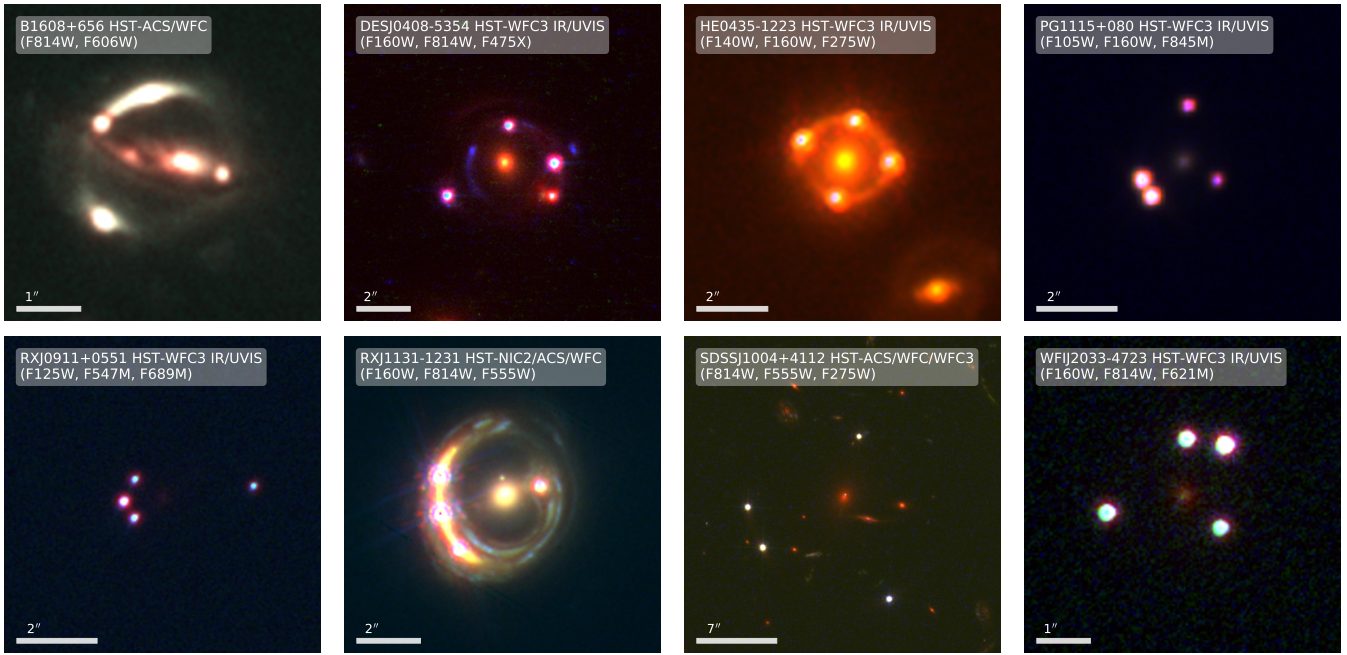


Figure 2. Composite HST images of the modelled lens systems centred on the main lens. The image data were stacked using 2 or 3 bands in the UV/Visible, optical, or near-infrared with an individually modified method described by [Lupton et al. \(2004\)](#). The exact camera system and filters are listed in the label ordered by R, G, and B colour channels. In all images north is up and east is left.

2.3 HE0435-1223

[Wisotzki et al. \(2002\)](#) reported the discovery of this system. It has a lensed QSO at redshift $z_s = 1.689$ in a crossed image configuration. The redshift $z_l = 0.454$ of the lensing galaxy was measured three years later by [Morgan et al. \(2005\)](#), and time delays were reported the following year by [Kochanek et al. \(2006\)](#) as $\Delta t_{AC} = -2.1_{-0.71}^{+0.78}$, $\Delta t_{AD} = -14.37_{-0.82}^{+0.75}$, and $\Delta t_{AB} = -8.0_{-0.82}^{+0.73}$. The system has recently been the focus of many studies by the HOLiCOW collaboration which provided a spectroscopic survey ([Sluse et al. 2017](#)), a mass model ([Wong et al. 2016](#)), newly measured time delays ([Bonvin et al. 2017](#)), and external convergence field models ([Tihhonova et al. 2018](#)). Moreover, [Nierenberg et al. \(2017\)](#) investigated the lens' substructure with a WFC3 grism narrow-line survey. Recently [Millon et al. \(2020a\)](#) estimated the time delays as $\Delta t_{AB} = -9.0_{-0.8}^{+0.8}$, $\Delta t_{AC} = -0.8_{-0.7}^{+0.8}$, $\Delta t_{AD} = -13.8_{-0.8}^{+0.8}$, $\Delta t_{BC} = 7.8_{-0.9}^{+0.9}$, $\Delta t_{BD} = -5.4_{-0.8}^{+0.9}$, and $\Delta t_{CD} = -13.2_{-0.8}^{+0.8}$ days with arrival-time order CADB.

2.4 PG1115+080

The so-called *triple quasar* is the second gravitational lens ever discovered [Weymann et al. \(1980\)](#). Only after its naming, it was shown that the seemingly brightest image was—according to generic lens theory—in fact a blend of two separate images. The elliptical lensing galaxy was detected only 7 years after its discovery by [Christian et al. \(1987\)](#). [Kundic et al. \(1997\)](#) and [Tonry \(1998\)](#) independently measured the redshift of the lens to be $z_l = 0.311$. The potential to constrain cosmological parameters was realized early and time delays were first measured by [Schechter et al. \(1997\)](#), and soon after improved by [Barkana \(1997\)](#). The latest time delays were reported by ([Bonvin et al. 2018](#)) as $\Delta t_{AB} = 8.3_{-1.6}^{+1.5}$,

$\Delta t_{AC} = 9.9_{-1.1}^{+1.1}$, and $\Delta t_{BC} = 18.8_{-1.6}^{+1.6}$ days with arrival-time order CA_1A_2B .

2.5 RXJ0911+0551

[Bade et al. \(1997\)](#) confirmed this system to be gravitationally lensing after follow-up observations of candidates from the ROSAT All-Sky Survey (RASS). It shows a complex image configuration with one image particularly far from the other three, requiring a large external shear component [Burud et al. \(1998\)](#). It was suspected that the origin of the high shear was a nearby cluster, which was finally discovered two years later by [Kneib et al. \(2000\)](#). [Hjorth et al. \(2002\)](#) measured a time delay of $\Delta t_{AB} = 146_{-8}^{+8}$ days with arrival-time order $BA_1A_2A_3$, where B is the distant and leading component image, and A_i the combination of the other three.

2.6 RXJ1131-1231

The system has been serendipitously unveiled during polarimetric imaging of radio quasars by [Sluse et al. \(2003\)](#). The redshifts of the lens and source were measured as $z_l = 0.295$ and $z_s = 0.658$ ([Sluse et al. 2007](#)). HST imaging shows a detailed Einstein ring from the host galaxy of the multiply imaged quasar. Substructure-analyses by [Claeskens et al. \(2006\)](#) and [Suyu et al. \(2013\)](#) furthermore point out a satellite of the lensing galaxy, identifiable as a small, bright spot north of the lens. An extensive time delay estimation was obtained from a 9-year optical monitoring using three different numerical methods between all possible pairs of quasar images with arrival-time order BCAD by ([Tewes et al. 2013](#)). Due to the high quality of observational data available, the system has been subjected to modelling methods and cosmographic anal-

yses in many previous works (e.g. Holanda 2016; Birrer et al. 2016, 2017; Suyu et al. 2017).

2.7 SDSSJ1004+4112

With its multiple quasar images at a separation of 14.62'', this system is the largest and rarest object in our set (Inada et al. 2003). As expected from such a giant, it was shown to be a cluster dominated by dark matter (Oguri et al. 2004; Williams & Saha 2004). Since time delays are of the order of $c^{-3}GM$ it is only natural to expect much higher delays for cluster lenses. Oguri (2010) used mass models of the lensing galaxies to predict time delays of $\Delta t_{AD} \sim 1218$ days and Mohammed et al. (2015) demonstrated how useful such a time delay measurement would be for constraining its substructure. After more than 3.5 years of data collection the time delays were estimated as $\Delta t_{BA} = 40.6^{+1.8}_{-1.8}$, $\Delta t_{CA} = 821.6^{+2.1}_{-2.1}$, and $\Delta t_{AD} > 1250$ days with arrival-time order CBAD (Fohlmeister et al. 2008, 2007).

2.8 WFIJ2033-4723

Very similar to B1608+656 (see 2.1) and PG1115+080 (see 2.4), WFIJ2033-4723 is a quad in a fold configuration with two images almost blending. It was discovered by Morgan et al. (2004) during an optical imaging ESO survey. The quasar images are considerably brighter than the foreground lens galaxy whose redshift $z_1 = 0.661$ was measured by Eigenbrod et al. (2006). The redshift of the quasar images $z_s = 1.662$ were confirmed by Sluse et al. (2012b). The most recent time delay measurements report $\Delta t_{AB} = 36.2^{+0.7}_{-0.8}$, $\Delta t_{AC} = -23.3^{+1.2}_{-1.4}$, and $\Delta t_{BC} = -59.4^{+1.3}_{-1.3}$ days with arrival-time order BA₁A₂C (Bonvin et al. 2019).

3 LENS RECONSTRUCTION METHOD

The lenses were reconstructed using the free-form modelling code GLASS¹ (Coles et al. 2014) plus recent developments by Denzel et al. (2020). GLASS has previously been used for several studies of galaxy lenses (Coles et al. 2014; Küng et al. 2015; Bruderer et al. 2016; Küng et al. 2018) and cosmological parameters (Lubini et al. 2014) although not for H_0 , other than the TDLMC. However the related older code PixeLens² has been used to estimate H_0 (Saha & Williams 2004; Sereno & Paraficz 2014; Saha et al. 2006b).

3.1 GLASS

To formulate the method, we introduce the usual dimensionless density κ and arrival time τ

$$\begin{aligned} \Sigma(\boldsymbol{\theta}) &= \frac{c^3}{4\pi G H_0} \frac{d_L d_S}{d_{LS}} \kappa(\boldsymbol{\theta}) \\ H_0 t(\boldsymbol{\theta}) &= (1 + z_L) \frac{d_L d_S}{d_{LS}} \tau(\boldsymbol{\theta}) \end{aligned} \quad (6)$$

where d_L is D_L with the dimensional factor c/H_0 taken out. In terms of these, the arrival time becomes

$$\tau(\boldsymbol{\theta}) = \boldsymbol{\theta} \cdot \boldsymbol{\beta} + \frac{1}{2} |\boldsymbol{\theta}|^2 - 2\nabla^{-2} \kappa(\boldsymbol{\theta}). \quad (7)$$

In free-form or pixellated lens reconstruction, the mass distribution

$$\kappa(\boldsymbol{\theta}) = \sum \kappa_n Q(\boldsymbol{\theta} - \boldsymbol{\theta}_n) \quad (8)$$

is represented as a collection of pixels where $Q(\boldsymbol{\theta} - \boldsymbol{\theta}_n)$ is a square (or other profile) and $\boldsymbol{\theta}_n$ is its centroid. The contribution $\nabla^{-2} Q(\boldsymbol{\theta})$ of a square to the arrival time can be calculated analytically (AbdelSalam et al. 1998).

The pixels κ_n are arranged in concentric ‘pixel rings’ centred on the lensing galaxy. The central pixel can be refined into sub-pixels in order to better resolve steep cusps. The κ_n values are required to satisfy the following prior inequality constraints.

- (i) All mass densities must be non-negative: $\kappa_n \geq 0$.
- (ii) In order to keep the mass distribution relatively smooth, no mass tile can exceed twice the average of its neighbors.
- (iii) The local density gradient $\nabla \kappa$ should point within $\alpha = 60^\circ$ of radially inwards:

$$\mathbf{R} \nabla \kappa \geq 0, \quad \mathbf{R}^\top \nabla \kappa \geq 0$$

where $\mathbf{R} = \mathbf{R}(\alpha)$ is a rotation.

- (iv) The average density $\langle \kappa \rangle_i$ of mass within a ring i at radius R_i must have a profile that is steeper than R^{-s} :

$$R_i^{-s} \langle \kappa \rangle_i - R_{i+1}^{-s} \langle \kappa \rangle_{i+1} \geq 0$$

This still allows for twisting iso-density contours and significantly varying ellipticities with radius. In this work we set $s = 0$, requiring only that the circularly averaged surface mass density does not increase with radius, which is rather conservative.

Additionally, since the pixels cover only a relatively small, finite surface, external shear from, e.g., a nearby galaxy, can be added to Eq. (7), as a two-component shear

$$\gamma_1 (\theta_x^2 - \theta_y^2) + 2\gamma_2 \theta_x \theta_y \quad (9)$$

where (γ_1, γ_2) are constant shear components. Furthermore, neighbouring galaxies can be modelled as point masses (or other distributions) whose contributions also add to Eq. (7).

Multiple-image data from observations further constrain the mass distribution:

- (i) The arrival time must be stationary at the observed image locations. That is, for all image locations $\boldsymbol{\theta}_i$ we require $\nabla \tau(\boldsymbol{\theta}_i) = 0$. For one image, such an equation simply relates the unknown source position to the image position, so it does not constrain the mass distribution. Additional images from the same source do, however, constrain the mass distribution, because the source position has already been determined by the first image.
- (ii) The elements of the inverse magnification tensor $\nabla \nabla \tau(\boldsymbol{\theta})$ are constrained by inequalities to enforce supplied image parities. These are not known a priori, but have to be inferred by the investigator based on the brightness of the images, time-delay data, and test runs.

¹ GLASS: <http://ascl.net/1806.009>

² PixeLens: <https://ascl.net/1102.007>

- (iii) The time delay $\tau(\theta_i) - \tau(\theta_j)$ between images must reproduce the observed time delays.

These equality and inequality constraints are all linear in the mass tiles κ_n , the source position β , the external shear components γ_1, γ_2 , any additional point masses, and finally H_0 . As a result, in the high-dimensional space of these quantities, there is a convex polytope inside which all points satisfy the prior and data constraints. Lubini & Coles (2012) developed an algorithm for uniformly sampling high-dimensional polytopes, which is implemented in GLASS. The following definitions are used in GLASS modelling:

- A lensing mass Σ is made up of ~ 200 pixels, whose values are individually adjustable subject to the constraints discussed above.
- A *model* is the set of a mass distributions Σ_i , shear terms, etc. for all eight lenses which reproduce the respective image and time-delay data and share a common value for H_0 .
- An *ensemble* is a set of 1000 models drawn uniformly from the space of solutions that satisfy the above constraints.

A detailed discussion of the method and prior is given by Coles (2008), and the consequences of the various assumptions have been studied in previous works such as Lubini et al. (2014); Küng et al. (2015); Denzel et al. (2020).

3.2 Point-image data

Table 1 lists the point-image and time-delay data used in this study. We also indicate the locations of external galaxies approximated as point masses.

The following settings were also used.

- The mass pixels were arranged in a discretised circular disc 17 pixels in diameter. The central pixel was further refined into 3×3 sub-pixels. The side length of the mass pixels was between $0.19''$ and $0.35''$ with SDSSJ1004+4112 being an exception at $1.4147''$. Note that $\tau(\theta)$ is not discretised.
- All models allowed for external shear.
- A flat cosmology with $(\Omega_m, \Omega_\Lambda) = (0.27, 0.73)$ was assumed.

3.3 Extended image data

The procedure thus far uses solely the centroidal positions of the multiply imaged quasars. We now incorporate the full photometric data of the extended images as described in Denzel et al. (2020) and related earlier work (Küng et al. 2018).

As images appear where $\nabla\tau(\theta) = 0$, we first define a lens mapping $L(\theta, \beta)$, which is equivalent to the more commonly known lens equation. An extended image produced by an extended source can then be written as

$$I(\theta) = \int L(\theta, \beta) S(\beta) d^2\beta. \quad (10)$$

For each of the 1000×8 lens masses in an ensemble we generate synthetic images by fitting a source brightness distribution $S(\beta)$ such that the extended image I further convolved by a point spread function $P(|\theta - \theta'|)$

$$\int P(|\theta - \theta'|) L(\theta', \beta) S(\beta) d^2\theta' d^2\beta \quad (11)$$

optimally fits the data. The extended image is linear in the source brightness distribution, so fitting is straightforward.

3.4 Lessons from the TDLMC

In January 2018, the Time Delay Lens Modelling Challenge was initiated. Ding et al. (2018) explained the experimental design and invited scientists to model 50 simulated Hubble Space Telescope (HST) observations of mock lens systems. The challenge was divided into three ‘rungs’ each featuring a set of 16 lenses which increased in modelling difficulty. Additionally, the ‘Evil’ team, the designers of the challenge, provided a calibration rung containing 2 lenses along with the entire information about the systems. For all other lenses, an HST mock image of the lens, the redshifts of source and lens, external convergence estimates, velocity dispersion estimates, the time delays, a noise map, and a point-spread function (PSF) map were provided. Based on this information, the challenge for the ‘Good’ teams was to infer H_0 , which was randomly fixed between 50 and $90 \text{ km s}^{-1} \text{ Mpc}^{-1}$ by the Evil team, for each rung for a fixed background cosmology. With final submission on September 8th 2019, the TDLMC finished its submission phase, and the results were thoroughly evaluated (Ding et al. 2020).

We have participated in this challenge and were able to test our free-form modelling techniques extensively with focus on H_0 inference beforehand. Lessons learned from the challenge influenced the present work in several ways.

Tests on simulated data always come with some caveats. In particular, mock lenses in rung3 were derived from hydrodynamical simulations of galaxies. Expectedly, this limits the quality of mock lenses to the one of the used simulations. In particular, the resolution of the galaxies were known to be insufficient to resolve the inner regions of the galaxies. Some of the limitations on the other hand were discovered post-unblinding, such as inconsistencies with the kinematics due to the removal of substructure, and the halo truncation at the virial radius, which does not follow isodensity contours and potentially biases H_0 .

More importantly, during the challenge we have noticed that the simulated lenses differ from observed ones in at least one important aspect: the radial spread of the images around the lens center is considerably wider, by about a factor of 2, in observed lenses compared to the simulated ones (also see Gomer & Williams 2020, in preparation). This leads us to expect that the lens sample from this work should yield more precise results on the inference of H_0 . In the last paragraph of Subsection 4.4 and Figure 11 we present the accuracy and precision of our TDLMC results, and compare the precision to that of the present work.

Our TDLMC participation was also helpful in guiding the modelling procedure carried out in this paper. The most striking conclusion we drew from our TDLMC participation was that as soon as double systems entered the analysis, our H_0 inference tended to much lower and less accurate values; at times even lower than the asserted range of possible values. After rung1 however, we decided to include a joint-analysis containing only quad systems, besides other combinations of quads and doubles. The best results were achieved this way and are shown as histograms of our H_0 posteriors in Figure 11. This was the main reason why only quad systems were selected for the sample presented in this work.

System	Labels	x, y [arcsec]	z_L	z_S	Time delays [days]	Point mass x, y [arcsec]	Reference	
B1608+656	B	(-0.82, 1.28)	0.63	1.39		(0.14, 0.79)	(1); (2); (3); (4)	
	A	(1.10, 0.42)						31.5 ± 1.5,
	C	(0.68, 1.20)						4.5 ± 1.5,
	D	(-0.23, -0.64)						41 ± 1.5
DESJ0408-5354	A	(1.25, -2.15)	0.597	2.375			(5); (6)	
	B	(0.04, 1.86)						112.1 ± 2.1,
	C	(1.26, 1.77)						155.5 ± 12.8 [†] ,
	D	(-1.37, 0.15)						42.4 ± 17.6 [‡]
HE0435-1223	C	(1.35, -0.36)	0.454	1.689			(7); (8); (9); (10)	
	A	(-1.18, -0.07)						2.1 ± 0.78,
	D	(-0.06, -1.09)						6 ± 1.07,
	B	(0.19, 1.13)						8.37 ± 1.31
PG1115+080	C	(0.11, 1.37)	0.311	1.735			(11); (12); (13); (14)	
	A ₁	(-0.79, -0.87)						13.3 ± 0.9,
	A ₂	(-1.06, -0.43)						11.7 ± 1.5
	B	(0.86, -0.46)						
RXJ0911+0551	B	(-2.27, 0.29)	0.769	2.763		(-0.76, 0.66)	(15); (16); (17); (18)	
	A ₁	(0.96, -0.10)						146 ± 8,
	A ₂	(0.70, -0.50)						
	A ₃	(0.69, 0.46)						
RXJ1131-1231	B	(1.39, 1.64)	0.295	0.658		(0.51, -0.14)	(7); (19); (20); (21); (22); (12)	
	C	(-0.96, 2.06)						1.50 ± 2.49,
	A	(0.29, 2.13)						9.61 ± 1.97,
	D	(-0.23, -1.18)						87 ± 8
SDSSJ1004+4112	C	(8.85, -4.44)	0.68	1.74			(23); (24); (25); (26); (27)	
	B	(-5.76, -6.36)						821.6 ± 2.1,
	A	(-2.46, -8.19)						40.6 ± 1.8,
	D	(-2.37, 4.64)						
WFIJ2033-4723	B	(0.60, 1.35)	0.661	1.66			(28); (29); (30)	
	A ₁	(0.31, -1.21)						35.5 ± 1.4,
	A ₂	(0.86, -0.66)						
	C	(-0.88, -0.23)						27.1 ± 1.4

Table 1. Input parameters used to model the gravitational lens systems. The images of each lens are ordered according to arrival times (earliest on top). Time delays have been recalculated accordingly. If not otherwise indicated, all time delays are with respect to the previous image. Image coordinates x, y are relative to the center of the lensing galaxy. The measured redshifts z_L and z_S correspond to the lens and source redshifts. To account for any significant external lensing contribution (besides external shear), we added point masses at the positions where galaxies of similar redshift are visible in the field. Every lens has been subjected to rigorous investigations in the past as explained in Section 2; the references to the works used particularly in this study are cited here: (1) Koopmans & Fassnacht (1999); (2) Fassnacht et al. (1999b); (3) Fassnacht et al. (2002); (4) Koopmans et al. (2003); (5) Lin et al. (2017); (6) Courbin et al. (2018); (7) Millon et al. (2020a); (8) Bonvin et al. (2017); (9) Sluse et al. (2012a); (10) Kochanek et al. (2006); (11) Morgan et al. (2008); (12) Tonry (1998); (13) Barkana (1997); (14) Weymann et al. (1980); (15) Eulaers & Magain (2011); (16) Hjorth et al. (2002); (17) Burud et al. (1998); (18) Bade et al. (1997); (19) Birrer et al. (2016); (20) Tewes et al. (2013); (21) Sluse et al. (2007); (22) Sluse et al. (2003); (23) Fohlmeister et al. (2007); (24) Fohlmeister et al. (2008); (25) Williams & Saha (2004); (26) Oguri et al. (2004); (27) Inada et al. (2003); (28) Bonvin et al. (2019); (29) Eigenbrod et al. (2006); (30) Morgan et al. (2004).

†: With respect to the first image. ‡: With respect to the second image.

4 RESULTS

Most of the results in this paper come from an ensemble of 1000 eight-lens models required to reproduce the point-image and time-delay data. This ensemble was also subsequently filtered according to how well extended images could be reproduced. We consider the average of the ensemble, and also the variation within the ensemble. Because the model ensemble is constructed using linear constraints, any weighted average of ensemble members is also a valid model.

Apart from the main ensemble, we produced two further models using the same image and time-delay data, but constrained to the H_0 values from Planck and SH0ES mentioned at the beginning of this paper, to demonstrate their compatibility. Furthermore, we compare distribution of inferred H_0 to models for the mock data from the TDLMC in Subsection 4.4.

4.1 Arrival-time surfaces

Figure 3 shows contour maps of the arrival time $\tau(\boldsymbol{\theta})$ from the average models of the main ensemble. The orientation in this figure is different from Figure 2 but consistent with subsequent figures. In the classification of [Saha & Williams \(2003\)](#) HE0435-1223 is a core quad, RXJ1131-1231 a long-axis quad, RXJ0911+0551 a short-axis quad, while the rest are inclined quads. The minima and saddle point appear at the correct image locations, as required, and there are no indications of spurious additional images.

4.2 Convergence maps

Figure 4 shows convergence maps $\kappa(\boldsymbol{\theta})$ of the ensemble-average models. The maps exhibit the typical pixellated structure stemming from the free-form technique. Contrary to earlier work imposing inversion symmetry in most cases ([Saha et al. 2006a](#); [Paraficz & Hjorth 2010](#)) all the lens models allow for asymmetry, which seems to be an important feature, in e.g., DESJ0408-5354 and RXJ0911+0551. Rough shapes and orientations seem to agree with previous reconstructions ([Chantry et al. 2010](#); [Wynne & Schechter 2018](#); [Shajib et al. 2020](#); [Yoo et al. 2005](#); [Saha et al. 2007](#)). The area within the black contours on the maps indicate a supercritical density with $\kappa \geq 1$. This area defines a scale which can be expressed as the Einstein radius and formally corresponds to the radius where $\langle \kappa \rangle_{\text{RE}} = 1$.

In Figure 5 the value for the Einstein radius can easily be read off (as vertical lines). It shows the distribution of average enclosed κ as a function of radial distance from lens centre for the entire ensemble. The ensemble-average profile is depicted in red. As it is typical for (good) lens reconstructions, the spread in the Einstein radius is minimal and usually accurate due to the strong constraints coming from the images themselves which usually lie at comparable radii. Conversely, the spread within the ensemble towards center is much greater ranging from cored profiles to almost cusp-like centres. This too was expected due to the lack of constraints at these radii. Note that all profiles are in units of κ which is the surface density scaled to the critical density for each lens, giving them the appearance of having seemingly similar mass contents. Particularly for SDSSJ1004+4112, the masses exceed magnitudes of (normal) galaxies and clearly reach cluster scales.

Since free-form lens-reconstruction ensembles can in principle contain many differently shaped density maps, it is important to investigate dominant as well as secondary features across all models in an ensemble. As explained in Section 3, these models represent solutions from a high-dimensional space, treating each mass tile as a parameter. To do this we carried out a principal-components analysis (PCA) of the ensemble (similar to [Mohammed et al. 2015](#); [Küing et al. 2018](#)). A PCA yields a representation of the mass distribution for the k -th lens ($k = 1, 2, \dots, 8$) of the form

$$\kappa^{(k)}(\boldsymbol{\theta}) = \bar{\kappa}^{(k)}(\boldsymbol{\theta}) + \sum_p c_p \Delta \kappa_p^{(k)}(\boldsymbol{\theta}) \quad (12)$$

where $\bar{\kappa}^{(k)}$ is the ensemble-average lensing mass (as shown in Figure 4), while $\Delta \kappa_p^{(k)}$ is the p -th principal component, and c_p is a coefficient. The $\Delta \kappa_p^{(k)}$ are orthonormal by construction. Note that the coefficients c_p do not depend on k , but are common for all eight lenses. Each of the c_p has a range of values across the ensemble: the coefficient c_1 of the first

System	Date	χ^2	χ_{Planck}^2	χ_{SH0ES}^2
B1608+656	2004-08-24	1.24	1.22	1.26
DESJ0408-5354	2018-01-17	3.90	4.01	3.78
HE0435-1223	2011-04-11	3.88	3.70	3.88
PG1115+080	2013-03-23	1.99	1.90	1.99
RXJ0911+0551	2012-10-19	8.97	9.78	9.17
RXJ1131-1231	2004-06-24	8.18	9.63	8.94
SDSSJ1004+4112	2010-06-07	102.67	102.53	100.74
WFIJ2033-4723	2013-05-03	6.17	6.27	5.93

Table 2. Reduced χ^2 from the source-reconstruction fitting. The first column refers to least squares from the main ensemble model's average. χ_{Planck}^2 and χ_{SH0ES}^2 are the corresponding least squares from the ensembles which have been constrained to fixed values of H_0 from Planck and SH0ES.

principal component has the largest range, while c_{100} stays close to zero. Thus, PCA filters and sorts the ensemble for its most salient features. Figure 6 shows an example of lens models projected into the PCA-feature space. It considers the lens WFIJ2033-4723 and the 1st, 2nd, 5th, and 100th principal components. For each of these, we display the projection

$$\bar{\kappa}^{(k)}(\boldsymbol{\theta}) + c_p \Delta \kappa_p^{(k)}(\boldsymbol{\theta}). \quad (13)$$

for the 16th and 84th percentile values of c_p . This figure illustrates the variety of models within an ensemble, but concurrently also identifies regions in the convergence maps which have been constrained to a higher degree and thus have low variance. As observed in Figure 5, the convergence maps are typically well constrained around the notional Einstein ring (indicated by a black contour in Figures 4 and 6), since in most cases by the 5th principal component its shape already does not vary anymore.

4.3 Synthetic images

Another rather affirming result is presented by the synthetic images from source reconstructions using the ensemble-averaged lens models. In the least-squares fitting discussed in Subsection 3.3, a Poisson noise in the photometry was assumed $\sigma_{\theta}^2 = g^{-1} |D_{\theta}^{\text{obs}}|$ where g is the gain or counts per photon. The source reconstructions yielded reduced χ^2 which are listed in Table 2.

The reduced least-squares provide a standardized measure of the synthetic's quality. A $\chi^2 = 1$ means the synthetic image differs from the data only on noise level and provides an ideal fit. However, since the observations come from different camera systems, wavelength bands, and dates ranging from 2004 to 2018, the data contains various signal-to-noise ratios (SNR). Consequently, a χ^2 of say 1.5, is easier to reach for a relatively old and noisy image, compared to one taken with a more modern system with a lower SNR. The scatter of χ^2 within a lens system is typically only between 1 or 2, in the case of SDSSJ1004+4112 about 8. The least squares from the source reconstructions of the models which were constrained with values of H_0 from Planck and SH0ES (see Section 1) were labelled χ_{Planck}^2 and χ_{SH0ES}^2 .

The synthetic images from averages of the main ensemble for each lens are shown in Figure 7. Apart from a few

minor details, all lensed features have successfully been reconstructed with astonishingly low χ^2 (SDSSJ1004+4112 being an exception). In some cases, e.g. for B1608+656, RXJ0911+0551, and WFIJ2033-4723, the shape of the quasar images are slightly warped, perhaps due to too high shear components. In B1608+656 and WFIJ2033-4723, flux ratios between some of the quasar images also noticeably differ. RXJ1131+01231, although the quasar images and most of the fainter Einstein ring are fitted relatively well for this system, shows artifacts which contribute the majority of errors. The origin of the artifacts are unclear.

The synthetic image of SDSSJ1004+4112 shows much fainter images than the original. This probably comes from the fact that the cluster galaxies induce much higher deflection angles and therefore more space for errors than for much smaller strongly-lensing galaxy systems. Problems with SDSSJ1004+4112 were expected since it is a cluster lens with many details which have been missed during the modelling. The considerably higher χ^2 in Table 2 compared to the other systems are a sign of such problems. In part, the high χ^2 -values are explained by bad fits of the lower brightness regions around the notional Einstein radius. These differences are discernible in Figure 7 upon close inspection of the original and the synthetic image side by side. Another source of errors are the cluster galaxies which have not been masked properly.

4.4 H_0 posterior distribution

In Figure 8 and 9, the posterior distribution of values for H_0 and H_0^{-1} from the main ensemble model are depicted. These do not yet include constraints from the extended image data. We furthermore investigated whether the quality of source reconstructions correlated with H_0 . For this reason, we optimized the ensemble models in a post-processing step by calculating synthetic images for each model in the ensemble (as described in the previous subsection). Only a fraction of the models with the best overall χ^2 (excluding SDSSJ1004+4112) was kept and the rest discarded. Several fractions were tested, ranging from 10 to 80 per-cent. The H_0 posterior of the 30 per-cent-filtered ensemble is shown in Figure 1. Interestingly, this had no noticeable effect on the spread, no matter how many models were filtered out. This suggests that better source reconstructions of time-delay lenses will not place tighter constraints on H_0 . In particular, Figure 1 shows the median of the distributions at

$$H_0 = 2.33_{-0.11}^{+0.13} \text{ aHz} = 71.8_{-3.3}^{+3.9} \text{ km s}^{-1} \text{ Mpc}^{-1}$$

and

$$H_0^{-1} = 13.7_{-0.7}^{+0.7} \text{ Gyr},$$

each at 68% confidence.

The Hubble constant is also equivalent to the cosmological critical density ρ_c (see 2). The distribution of ρ_c values in the main ensemble is displayed in Figure 10 in units of GeV/m^3 . Its median has a value of $\rho_c = 5.4_{-0.5}^{+0.6} \text{ GeV m}^{-3}$, at 68% confidence. For values of H_0 ranging from 60 to $80 \text{ km s}^{-1} \text{ Mpc}^{-1}$ the critical density corresponds to roughly 1 to 2 alpha particles per cubic metre. This is the quantity which should be compared to the early measurements, as those generally constrain H_0 through the baryon or matter densities $\propto H_0^2$.

The spread in the distribution of H_0 is large, in fact the ensemble contains solutions ranging from 60 to more than $80 \text{ km s}^{-1} \text{ Mpc}^{-1}$. This means that any value of H_0 is in principle consistent with the data constraints and priors. The reason for this lies for the most part in how the free-form technique builds convergence maps. It explores the degenerate solution space for the lens equation coupled with a few physical and regularization priors. At first, this spread could imply that the solutions have not been properly constrained or regularized. However, as shown in the previous Subsection 4.3, the models are able to reproduce the extended lens photometry quite well (with only one exception). This suggests that the models are in fact on average physically viable. Note that the extended lens photometry didn't go into the modelling process.

Another interesting observation about the H_0 distribution is that its error distribution does not appear to be Gaussian, in fact the distribution in Figure 1 is clearly asymmetric. In astronomy, most analyses generally use a Gaussian error distribution, firstly, because of the central limit theorem, and secondly, because the assumption simplifies the estimation of unknown parameters. However, with realistic data, we do not know the probability distribution of the errors, nor whether it has any concrete mathematical form consistent from one observation to another. The wings of a Gaussian fall off quickly, meaning two or three σ residuals are very unlikely to occur. From experience, however, we know such deviations are far more common. Thus, an error distribution such as a Lorentzian or a Voigt profile which have a well-defined peak with wider wings, might be more reasonable estimates for realistic data. Even more flexible is the Tukey g-and-h (Yan & Genton 2019) distribution which allows for asymmetric wings. Gaussian distributions arise naturally when a quantity is a sum of many independent contributions and physical processes. Thus noise is typically Gaussian, and so are measurements that are signals on top of noise. The inference of the Hubble constant from observations of several lenses cannot, however, be decomposed into signal plus noise. Hence the uncertainty in H_0 is not in general Gaussian, and one can expect non-Gaussian properties such as skewness and kurtosis to be important. Likewise, a 1 per-cent determination of the Hubble constant which implicitly uses Gaussian errors, might actually have overestimated the precision of the measurement.

Comparing the spread of the distribution of H_0 values in the present work, Figure 1 and 8, to the ones from the TDLMC, it is apparent that this it is considerably narrower. Part of the reason for this could be the difference in the radial spread of images around the lens center, mentioned in Subsection 3.4. If images are confined to a narrow band around the lens center, as in TDLMC quads, lensing degeneracies, like the steepness, or mass sheet degeneracy, will be more rampant. This is because a given observational uncertainty on time delays will lead to larger fractional uncertainty in more circular lenses which have smaller time delays, resulting in less constraining power, and a wider range of derived H_0 values. Observed quads span a wider range of radial image positions, resulting in narrower H_0 distributions.

While our TDLMC models have a very large spread across the entire range of possible H_0 values, their median H_0 seems to determine the truth values quite accurately. This does not

mean that our techniques are able to consistently recover the truth values, but it still shows potential.

5 CONCLUSION

The Hubble constant has come a long way from the value of $\sim 500 \text{ km s}^{-1} \text{ Mpc}^{-1}$ implied by the historic Figure 1 in [Hubble \(1929\)](#). [Sandage \(1958\)](#) had improved the measurement to $H_0 \approx 75 \text{ km s}^{-1} \text{ Mpc}^{-1}$ or $H_0^{-1} \approx 13 \text{ Gyr}$ with an uncertainty of a factor of two. Debates over a factor of two were still continuing in [Sandage & Tammann \(1982\)](#) versus [de Vaucouleurs & Corwin \(1985\)](#). Today, H_0 has been constrained to within 10 per-cent, but the debates between “low” and “high” values remain, as do the legacy units of $\text{km s}^{-1} \text{ Mpc}^{-1}$. In view of the continuing debate over the value of H_0 , lensing time delays as a technique for measuring H_0 are very interesting, because they span a variety of redshifts and are free of the “twilight zone” (see [Sandage & Tammann 1974](#)) characteristic of the distance-ladder methods.

In this paper, we have presented a determination of the Hubble constant $H_0 = 2.33^{+0.13}_{-0.11} \text{ aHz} = 71.8^{+3.9}_{-3.3} \text{ km s}^{-1} \text{ Mpc}^{-1}$ through the joint free-form modelling of eight time-delay lenses using the most recent observational data. This value is consistent with both early and late Universe studies. We further demonstrate this fact by modelling these lenses in secondary ensembles which have fixed values of H_0 typical for CMB-based and SNeIa-based methods. Accordingly, these secondary ensemble models exhibit just as many or few problems as the main lens ensemble. We have analysed the models based on their arrival-time surfaces, convergence maps, and circularly-averaged density profiles and have found only minor shortcomings. Furthermore, the models’ projection properties have been tested by generating synthetic images using the source-reconstruction method presented in [Denzel et al. \(2020\)](#). Thereby, we have extended our analysis to data which have not initially been employed in the lens reconstructions. The results of this test affirmed the physical validity of our models, and so, the synthetic images and thereby the entire photometric data are finally used to constrain the ensemble further in a post-processing step. This had no notable effect, suggesting that optimizations of source reconstructions only weakly constrain H_0 . In our study, we have not (yet) considered phase-space models, or stellar kinematics, which might be able to further constrain our models.

As of the time of writing, a 1% determination of H_0 through lensing has yet to be reported. Nevertheless, even if such a measurement existed, only several repetitions with different data sets could confirm the accuracy of these measurements. As already discussed in Subsection 4.4, when we assess data, it is entirely unknown what kind of error distribution can be assumed. Thus, only if several measurements of H_0 across different observations consistently reach a 1 per-cent level, they are robust against the choice of errors. However, the TDLMC ([Ding et al. 2020](#)) suggests that while many lens-modelling techniques excel in reconstructing simple simulations based on parametric models, but decrease in consistency when faced with more general lenses taken from galaxy-formation simulations. As cautioned in several works (e.g. [Gomer & Williams 2019](#); [Kochanek 2020](#)) due to lensing degeneracies a single family of models is able to reproduce the same lensing ob-

servables, but return different values of H_0 . Free-form techniques keep consistency in accuracy and precision when the complexity of the lens is increased, as expected from their greater flexibility.

Interestingly, our new estimate of H_0 improves upon the precision of our measurements reported in the TDLMC. In the challenge, the simulated quads appeared to be slightly rounder with very little variation in the radial distance of the images. The real observations considered in this study appear to have a larger variation. We conjecture that a wider radial distribution of the lensed images puts tighter constraints on the slope of the density profile, and therefore provides tighter constraints on the Hubble constant. From our experience in the TDLMC, we also conclude that the most accurate joint inference of H_0 comes from modelling only quad systems. In addition to the more elliptical lens-image separations, we have improved upon the TDLMC in precision by increasing the number of simultaneously modelled quad systems from 4 to 8. This implies that minor improvements might be possible by increasing the number of modelled systems alone, provided they contain new information which is able to further constrain H_0 .

It may turn out that in galaxy lenses degeneracies impose a limit which can hardly be broken, and results similar to H_0 reported in this study perhaps are the best we can hope to attain. If this turns out to be the case, time delays for galaxy lenses can still be useful, by reversing the problem and using them together with H_0 from other methods to constrain substructure in lenses ([Mohammed et al. 2015](#)).

The situation is different in cluster lenses. Recently, [Ghosh et al. \(2020\)](#) considered cluster lenses with a time-delay quasar (such as SDSS J1004+4112 in this work) but also hundreds of other lensed sources at many redshifts, making up ~ 1000 images in all. With that many lensing constraints (expected to be achieved by JWST), a 1% measurement of H_0 from lensing time delays appears feasible.

ACKNOWLEDGMENTS

We would like to thank the anonymous referee for useful suggestions which improved the paper. PD acknowledges support from the Swiss National Science Foundation. This research is based on observations made with the NASA/ESA Hubble Space Telescope obtained from the Space Telescope Science Institute (STScI), which is operated by the Association of Universities for Research in Astronomy, Inc., under NASA contract NAS 5–26555. These observations are associated with programs #10158, #15320, #12324, #12874, #9744, and #10509.

DATA AVAILABILITY

The data underlying this article are available at the STScI (<https://mast.stsci.edu/>; the unique identifiers are cited in the acknowledgements). The derived data generated in this research will be shared on request to the corresponding author.

REFERENCES

- Abbott B. P., et al., 2017, *Nature*, 551, 85
- Abbott T. M. C., et al., 2018a, *Phys. Rev. D*, 98, 043526
- Abbott T. M. C., et al., 2018b, *Monthly Notices of the Royal Astronomical Society*, 480, 3879
- AbdelSalam H. M., Saha P., Williams L. L. R., 1998, *MNRAS*, 294, 734
- Aghanim N., et al., 2018, Planck 2018 results. VI. Cosmological parameters ([arXiv:1807.06209](https://arxiv.org/abs/1807.06209))
- Agnello A., et al., 2017, *Monthly Notices of the Royal Astronomical Society*, 472, 4038
- Allahverdi R., et al., 2020, arXiv e-prints, [p. arXiv:2006.16182](https://arxiv.org/abs/2006.16182)
- Alsing J., Heavens A., Jaffe A. H., 2016, *Monthly Notices of the Royal Astronomical Society*, 466, 3272
- Anderson L., et al., 2012, *MNRAS*, 427, 3435
- Bade N., Siebert J., Lopez S., Voges W., Reimers D., 1997, *A&A*, 317, L13
- Barkana R., 1997, *The Astrophysical Journal*, 489, 21–28
- Birrer S., Amara A., Refregier A., 2016, *Journal of Cosmology and Astroparticle Physics*, 2016, 020–020
- Birrer S., Amara A., Refregier A., 2017, *Journal of Cosmology and Astroparticle Physics*, 2017, 037
- Birrer S., et al., 2020, TDCOSMO IV: Hierarchical time-delay cosmography – joint inference of the Hubble constant and galaxy density profiles ([arXiv:2007.02941](https://arxiv.org/abs/2007.02941))
- Blandford R., Narayan R., 1986, *ApJ*, 310, 568
- Bonvin V., et al., 2017, *MNRAS*, 465, 4914
- Bonvin V., et al., 2018, *Astronomy & Astrophysics*, 616, A183
- Bonvin V., et al., 2019, *Astronomy & Astrophysics*, 629, A97
- Bruderer C., Read J. I., Coles J. P., Leier D., Falco E. E., Ferreras I., Saha P., 2016, *MNRAS*, 456, 870
- Burud I., et al., 1998, *The Messenger*, 92, 29
- Chantry V., Sluse D., Magain P., 2010, *Astronomy & Astrophysics*, 522, A95
- Christian C. A., Crabtree D., Waddell P., 1987, *The Astrophysical Journal*, 312, 45
- Claeskens J.-F., Sluse D., Riaud P., Surdej J., 2006, *Astronomy & Astrophysics*, 451, 865
- Coles J., 2008, *The Astrophysical Journal*, 679, 17
- Coles J. P., Read J. I., Saha P., 2014, *MNRAS*, 445, 2181
- Collett T. E., Smith R. J., 2020, *Monthly Notices of the Royal Astronomical Society*, 497, 1654–1660
- Courbin F., et al., 2018, *Astronomy & Astrophysics*, 609, A71
- Denzel P., Mukherjee S., Coles J. P., Saha P., 2020, *Monthly Notices of the Royal Astronomical Society*, 492, 3885–3903
- Ding X., et al., 2018, Time Delay Lens Modeling Challenge: I. Experimental Design ([arXiv:1801.01506](https://arxiv.org/abs/1801.01506))
- Ding X., et al., 2020, Time Delay Lens modelling Challenge: II. Results ([arXiv:2006.08619](https://arxiv.org/abs/2006.08619))
- Eigenbrod A., Courbin F., Meylan G., Vuissoz C., Magain P., 2006, *Astronomy & Astrophysics*, 451, 759–766
- Eulaers E., Magain P., 2011, *Astronomy & Astrophysics*, 536, A44
- Fassnacht C. D., Womble D. S., Neugebauer G., Browne I. W. A., Readhead A. C. S., Matthews K., Pearson T. J., 1996, *The Astrophysical Journal*, 460
- Fassnacht C. D., Xanthopoulos E., Koopmans L. V. E., Pearson T. J., Readhead A. C. S., Myers S. T., 1999a, Measuring H_0 with CLASS B1608+656: The Second Season of VLA Monitoring ([arXiv:astro-ph/9909410](https://arxiv.org/abs/astro-ph/9909410))
- Fassnacht C. D., Pearson T. J., Readhead A. C. S., Browne I. W. A., Koopmans L. V. E., Myers S. T., Wilkinson P. N., 1999b, *ApJ*, 527, 498
- Fassnacht C. D., Xanthopoulos E., Koopmans L. V. E., Rusin D., 2002, *ApJ*, 581, 823
- Fassnacht C., et al., 2004, *Proceedings of the International Astronomical Union*, 2004, 311
- Fohlmeister J., et al., 2007, *The Astrophysical Journal*, 662, 62
- Fohlmeister J., Kochanek C. S., Falco E. E., Morgan C. W., Wambsganss J., 2008, *The Astrophysical Journal*, 676, 761–766
- Freedman W. L., Madore B. F., Scowcroft V., Burns C., Monson A., Persson S. E., Seibert M., Rigby J., 2012, *The Astrophysical Journal*, 758, 24
- Freedman W. L., et al., 2019, *The Astrophysical Journal*, 882, 34
- Gavazzi R., Treu T., Koopmans L. V. E., Bolton A. S., Moustakas L. A., Burles S., Marshall P. J., 2008, *The Astrophysical Journal*, 677, 1046–1059
- Ghosh A., Williams L. L. R., Liesenborgs J., 2020, *Monthly Notices of the Royal Astronomical Society*, 494, 3998
- Gilman D., Birrer S., Treu T., 2020, arXiv e-prints, [p. arXiv:2007.01308](https://arxiv.org/abs/2007.01308)
- Gomer M. R., Williams L. L. R., 2019, Galaxy-lens determination of H_0 : constraining density slope in the context of the mass sheet degeneracy ([arXiv:1907.08638](https://arxiv.org/abs/1907.08638))
- Hildebrandt H., et al., 2016, *Monthly Notices of the Royal Astronomical Society*, 465, 1454
- Hinshaw G., et al., 2013, *ApJS*, 208, 19
- Hjorth J., et al., 2002, *The Astrophysical Journal*, 572, L11–L14
- Holanda R., 2016, *Astroparticle Physics*, 84, 78
- Hubble E., 1929, *Proceedings of the National Academy of Science*, 15, 168
- Inada N., et al., 2003, *Nature*, 426, 810–812
- Kneib J.-P., Cohen J. G., Hjorth J., 2000, *The Astrophysical Journal*, 544, L35
- Knox L., Millea M., 2020, *Physical Review D*, 101
- Kochanek C. S., 2020, *Monthly Notices of the Royal Astronomical Society*, 493, 1725
- Kochanek C. S., Morgan N. D., Falco E. E., McLeod B. A., Winn J. N., Dembicky J., Ketzebach B., 2006, *The Astrophysical Journal*, 640, 47
- Koopmans L. V. E., Fassnacht C. D., 1999, *ApJ*, 527, 513
- Koopmans L. V. E., Treu T., Fassnacht C. D., Blandford R. D., Surpi G., 2003, *The Astrophysical Journal*, 599, 70
- Kundic T., Cohen J. G., Blandford R. D., Lubin L. M., 1997, *The Astronomical Journal*, 114, 507
- Küing R., et al., 2015, *MNRAS*, 447, 2170
- Küing R., et al., 2018, *MNRAS*, 474, 3700
- Lin H., et al., 2017, *The Astrophysical Journal*, 838, L15
- Lubini M., Coles J., 2012, *MNRAS*, 425, 3077
- Lubini M., Sereno M., Coles J., Jetzer P., Saha P., 2014, *MNRAS*, 437, 2461
- Lupton R., Blanton M. R., Fekete G., Hogg D. W., O’Mullane W., Szalay A., Wherry N., 2004, *Publications of the Astronomical Society of the Pacific*, 116, 133
- Millon M., et al., 2020a, COSMOGRAIL XIX: Time delays in 18 strongly lensed quasars from 15 years of optical monitoring ([arXiv:2002.05736](https://arxiv.org/abs/2002.05736))
- Millon M., et al., 2020b, arXiv e-prints, [p. arXiv:2006.10066](https://arxiv.org/abs/2006.10066)
- Mohammed I., Saha P., Liesenborgs J., 2015, *Publications of the Astronomical Society of Japan*, 67
- Morgan N. D., Caldwell J. A. R., Schechter P. L., Dressler A., Egami E., Rix H.-W., 2004, *The Astronomical Journal*, 127, 2617–2630
- Morgan N. D., Kochanek C. S., Pevunova O., Schechter P. L., 2005, *The Astronomical Journal*, 129, 2531
- Morgan C. W., Kochanek C. S., Dai X., Morgan N. D., Falco E. E., 2008, *The Astrophysical Journal*, 689, 755–761
- Myers S. T., et al., 1995, *The Astrophysical Journal*, 447
- Nierenberg A. M., et al., 2017, *Monthly Notices of the Royal Astronomical Society*, 471, 2224
- Oguri M., 2010, *Publications of the Astronomical Society of Japan*, 62, 1017
- Oguri M., et al., 2004, *The Astrophysical Journal*, 605, 78–97
- Paraficz D., Hjorth J., 2010, *ApJ*, 712, 1378
- Pietrzyński G., et al., 2019, *Nature*, 567, 200–203
- Refsdal S., 1964, *MNRAS*, 128, 307

- Refsdal S., 1966, *MNRAS*, **132**, 101
- Reid M. J., Pesce D. W., Riess A. G., 2019, *The Astrophysical Journal*, **886**, L27
- Riess A. G., et al., 2016, *The Astrophysical Journal*, **826**, 56
- Riess A. G., et al., 2018, *The Astrophysical Journal*, **861**, 126
- Riess A. G., Casertano S., Yuan W., Macri L. M., Scolnic D., 2019, *The Astrophysical Journal*, **876**, 85
- Saha P., 2000, *AJ*, **120**, 1654
- Saha P., Williams L. L. R., 2003, *The Astronomical Journal*, **125**, 2769
- Saha P., Williams L. L. R., 2004, *AJ*, **127**, 2604
- Saha P., Williams L. L. R., 2006, *ApJ*, **653**, 936
- Saha P., Courbin F., Sluse D., Dye S., Meylan G., 2006a, *Astronomy & Astrophysics*, **450**, 461
- Saha P., Coles J., Macciò A. V., Williams L. L. R., 2006b, *ApJ*, **650**, L17
- Saha P., Williams L. L. R., Ferreras I., 2007, *The Astrophysical Journal*, **663**, 29
- Sandage A., 1958, *ApJ*, **127**, 513
- Sandage A., Tammann G. A., 1974, *ApJ*, **190**, 525
- Sandage A., Tammann G. A., 1982, *ApJ*, **256**, 339
- Sandage A., Tammann G. A., Saha A., Reindl B., Macchetto F. D., Panagia N., 2006, *The Astrophysical Journal*, **653**, 843
- Schechter P. L., et al., 1997, *The Astrophysical Journal*, **475**, L85
- Schneider P., Sluse D., 2014, *A&A*, **564**, A103
- Scott D., 2018, The Standard Model of Cosmology: A Skeptic's Guide ([arXiv:1804.01318](https://arxiv.org/abs/1804.01318))
- Sereno M., Paraficz D., 2014, *MNRAS*, **437**, 600
- Shajib A. J., et al., 2020, *Monthly Notices of the Royal Astronomical Society*, **494**, 6072
- Sluse D., et al., 2003, *Astronomy & Astrophysics*, **406**, L43–L46
- Sluse D., Claeskens J.-F., Hutsemékers D., Surdej J., 2007, *Astronomy & Astrophysics*, **468**, 885
- Sluse D., Chantry V., Magain P., Courbin F., Meylan G., 2012a, *Astronomy & Astrophysics*, **538**, A99
- Sluse D., Hutsemékers D., Courbin F., Meylan G., Wambsgans J., 2012b, *A&A*, **544**, A62
- Sluse D., et al., 2017, *Monthly Notices of the Royal Astronomical Society*, **470**, 4838
- Suyu S. H., Marshall P. J., Auger M. W., Hilbert S., Blandford R. D., Koopmans L. V. E., Fassnacht C. D., Treu T., 2010, *The Astrophysical Journal*, **711**, 201
- Suyu S. H., et al., 2013, *The Astrophysical Journal*, **766**, 70
- Suyu S. H., et al., 2017, *MNRAS*, **468**, 2590
- Tewes M., et al., 2013, *Astronomy & Astrophysics*, **556**, A22
- Tihhonova O., et al., 2018, *Monthly Notices of the Royal Astronomical Society*, **477**, 5657
- Tonry J. L., 1998, *The Astronomical Journal*, **115**, 1–5
- Treu T., et al., 2018, *Monthly Notices of the Royal Astronomical Society*, **481**, 1041
- Wagner J., 2018, *A&A*, **620**, A86
- Weymann R. J., Latham D., Angel J. R. P., Green R. F., Liebert J. W., Turnshek D. A., Turnshek D. E., Tyson J. A., 1980, *Nature*, **285**, 641
- Williams L. L. R., Saha P., 2000, *AJ*, **119**, 439
- Williams L. L. R., Saha P., 2004, *The Astronomical Journal*, **128**, 2631–2641
- Wisotzki L., Schechter P. L., Bradt H. V., Heinmüller J., Reimers D., 2002, *Astronomy & Astrophysics*, **395**, 17
- Wong K. C., et al., 2016, *Monthly Notices of the Royal Astronomical Society*, **465**, 4895
- Wong K. C., et al., 2020, *Monthly Notices of the Royal Astronomical Society*
- Wynne R. A., Schechter P. L., 2018, Robust modeling of quadruply lensed quasars (and random quartets) using Witt's hyperbola ([arXiv:1808.06151](https://arxiv.org/abs/1808.06151))
- Yan Y., Genton M. G., 2019, *Significance*, **16**, 12
- Yoo J., Kochanek C. S., Falco E. E., McLeod B. A., 2005, *The Astrophysical Journal*, **626**, 51
- Young P., Gunn J. E., Kristian J., Oke J. B., Westphal J. A., 1980, *ApJ*, **241**, 507
- de Vaucouleurs G., Corwin H. G. J., 1985, *ApJ*, **297**, 23

6 FIGURES

This section contains all figures which are referenced in previous sections.

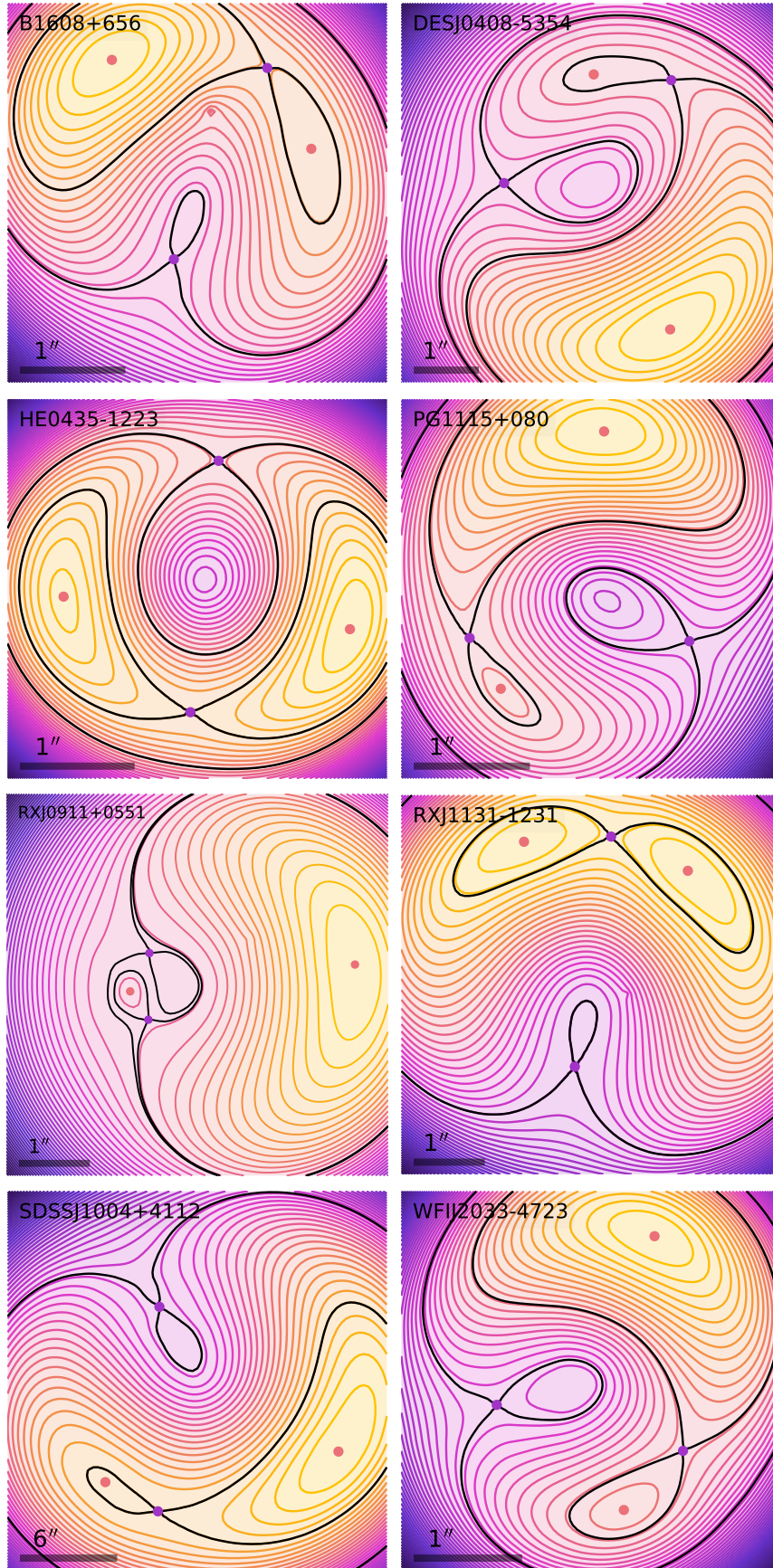


Figure 3. Arrival-time surfaces of the ensemble-average models. The image-position constraints with minimum and saddle parity are indicated by red and purple dots respectively. Contours passing through saddle points are in black. The scale bar on the lower left in each panel shows the angular scale in arcseconds. Orientations are at arbitrary rotation compared to Figure 2, but consistent with the following figures.

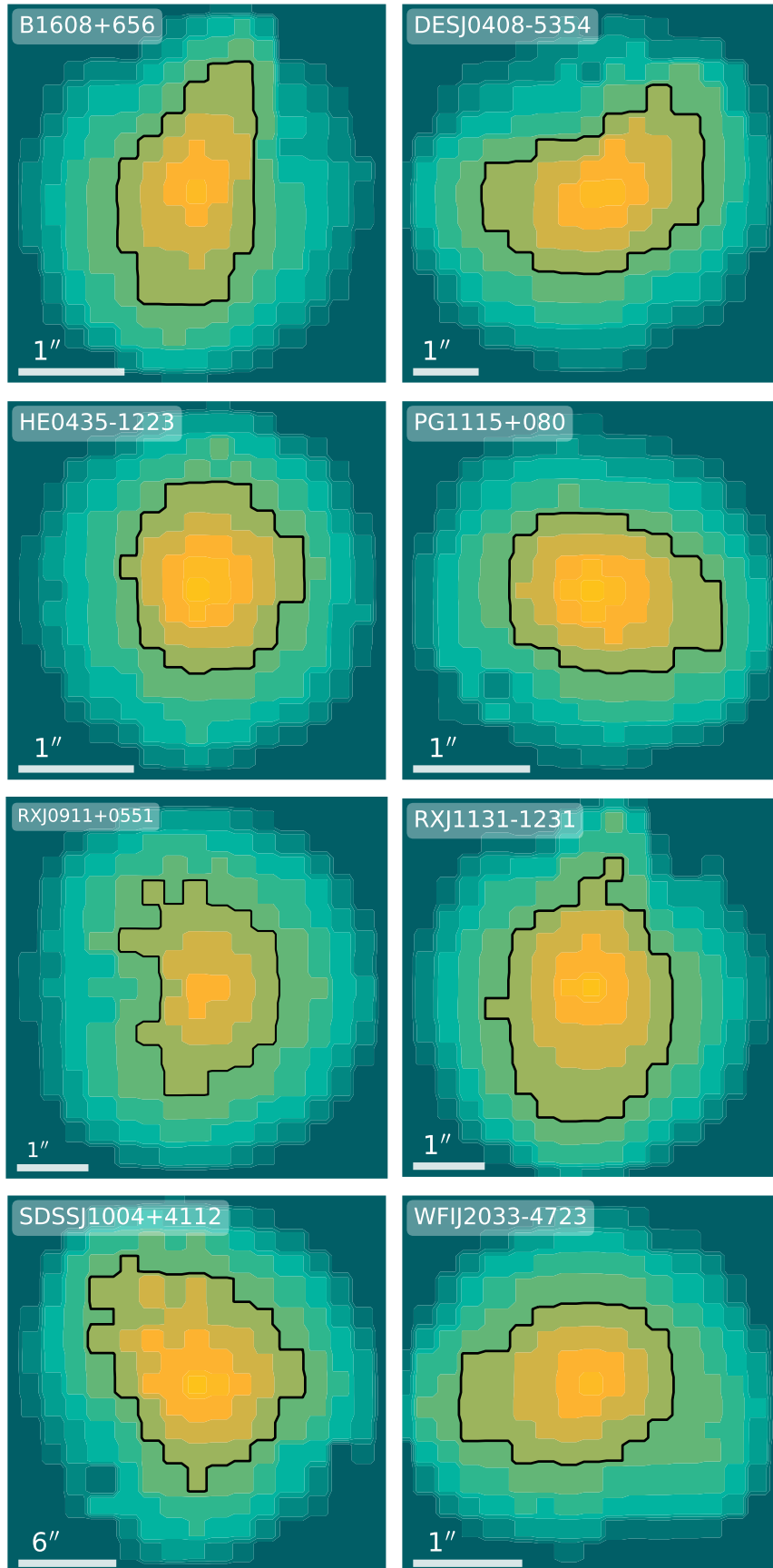


Figure 4. Model-convergence maps (ensemble averages) of all lenses. Black contours indicate a $\kappa = 1$. Scales and orientations are identical to the corresponding panels in Figure 3.

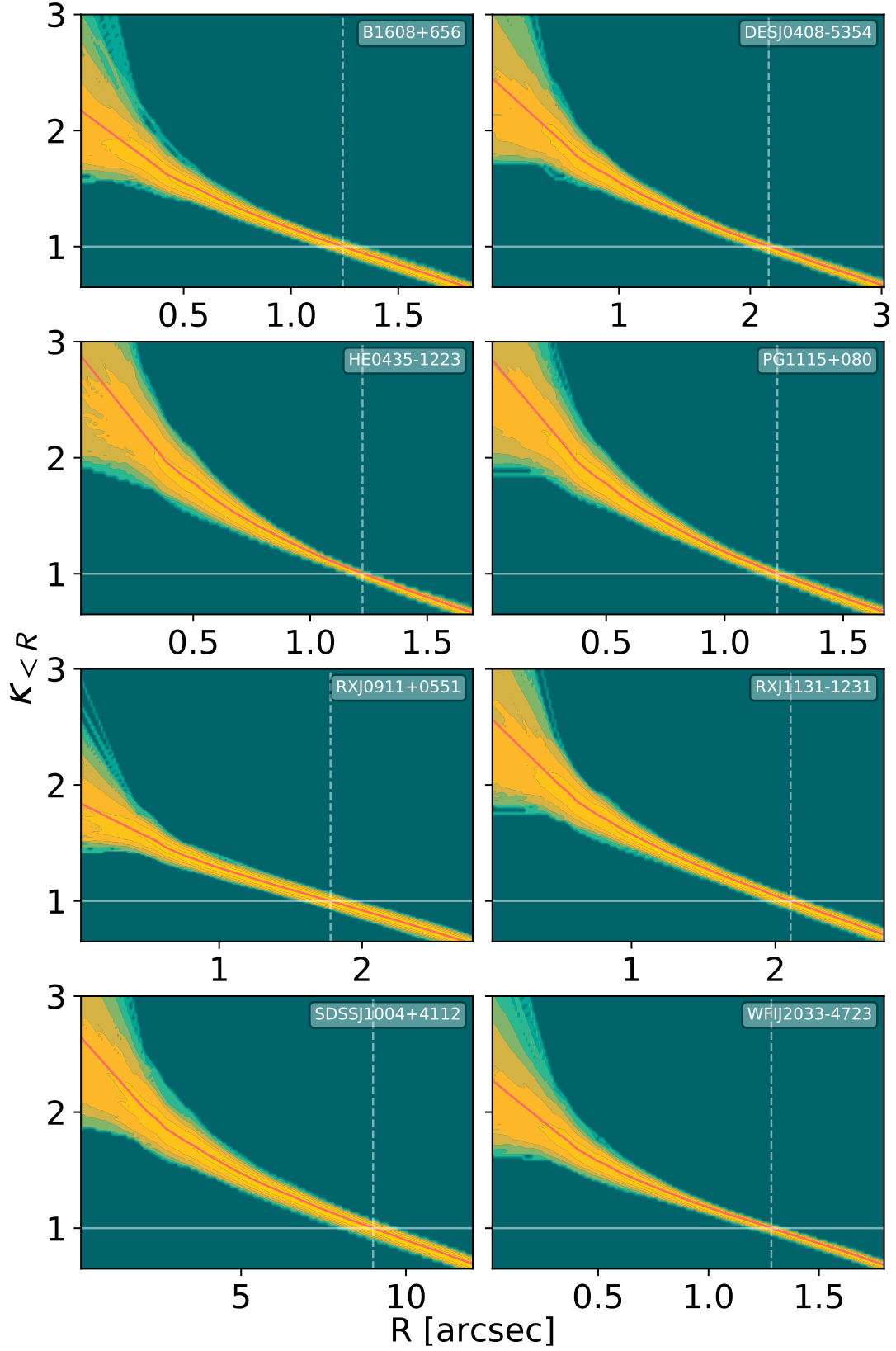


Figure 5. Radial profiles of the mean enclosed κ within a given projected radius from the centre of the modelled galaxy. The model ensemble is represented with a coloured region with a gradient from green to yellow indicating its number density of models. The red line describes the ensemble average. The vertical dashed line shows the notional Einstein radius (that is, the radius with mean convergence of unity) for the ensemble average.

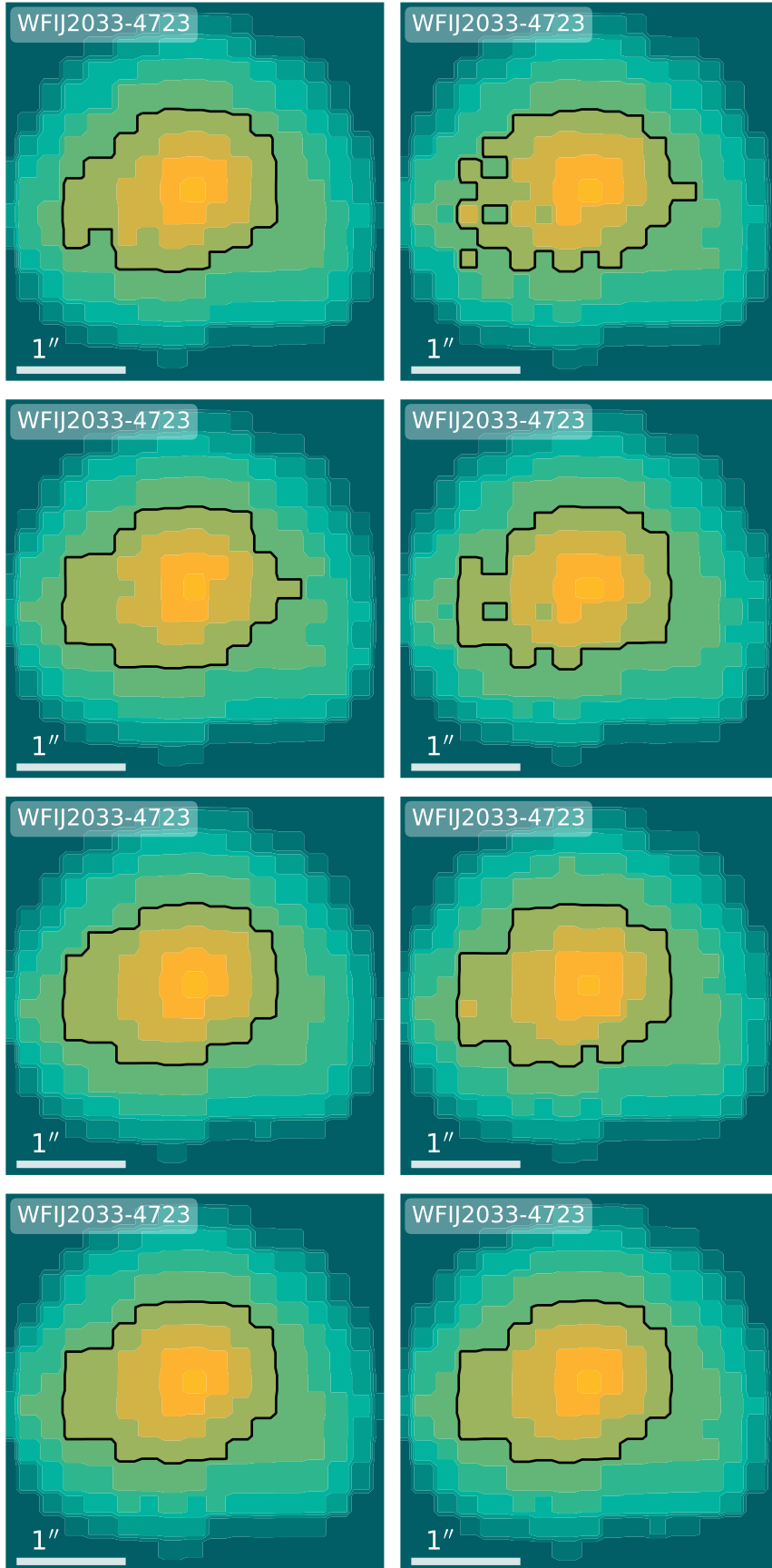


Figure 6. Variation of the convergence maps for WFIJ2033-4723 across the ensemble. (The ensemble average appears in the bottom-right panel of Figure 4.) The top row shows the 16th and 84th percentile projections along the first principal component. The other rows refer to the 2nd, 5th and 100th principal components. See text near Eq. (13) for details.

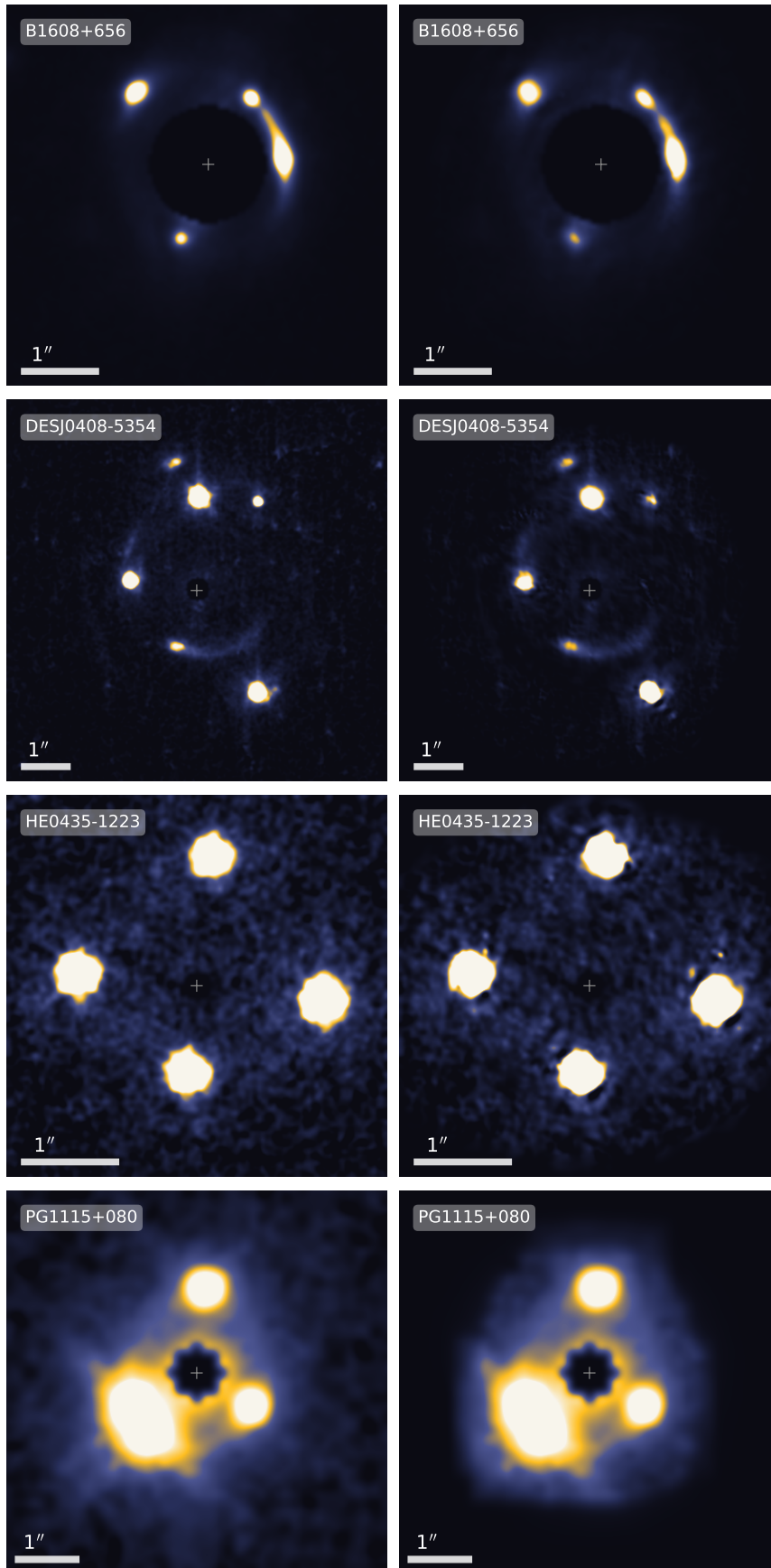
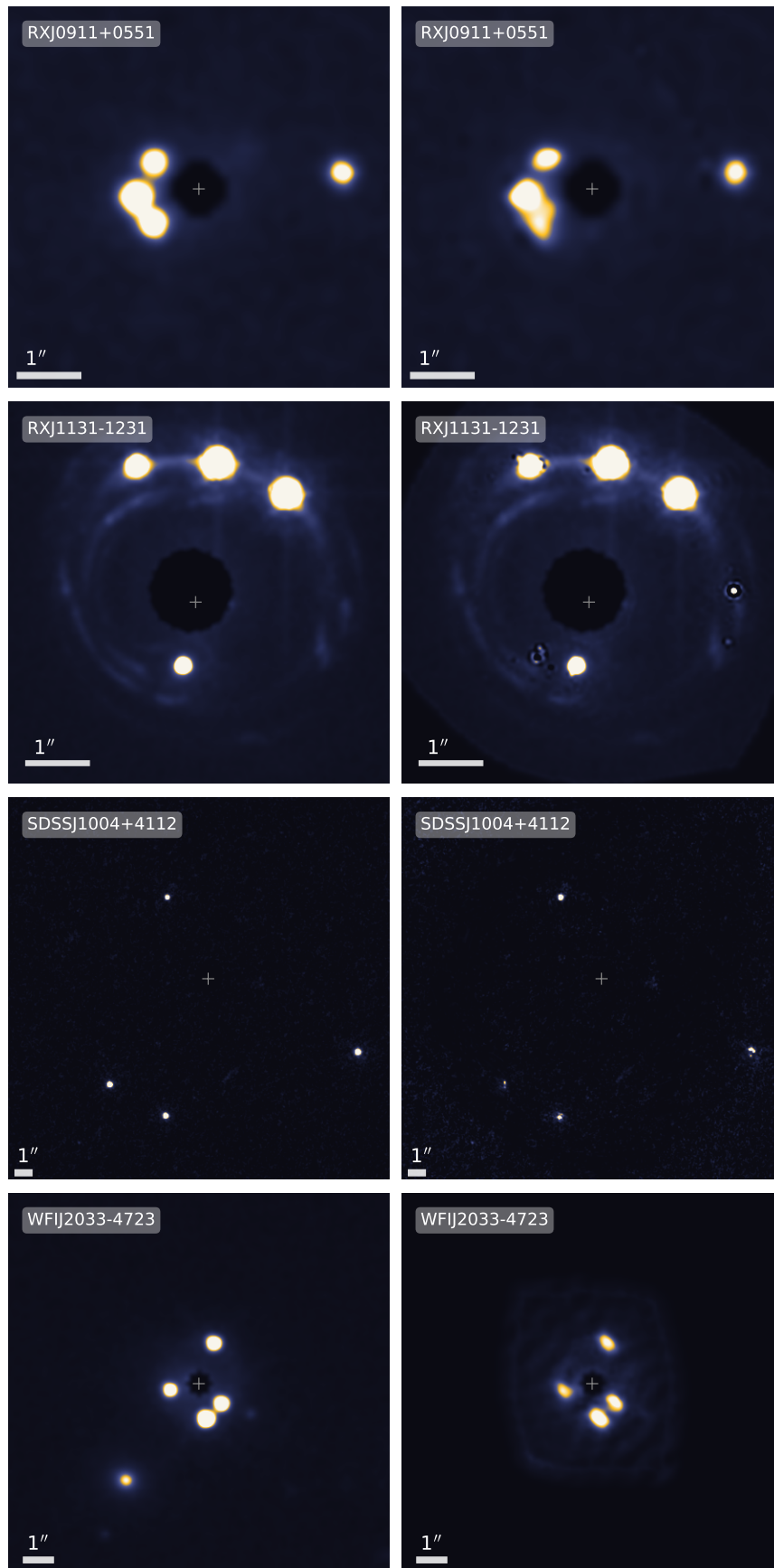


Figure 7. Photometric lens data and synthetic images produced using the ensemble-average model of each lens. The maps are in arbitrary units of brightness, but for each row adjusted to the same brightness levels. To avoid contamination of the lensed images by the lens light, a circular region around the lens has been masked with its center indicated by a cross and roughly corresponding to the modelled lens position. The scale bar on the lower left in each panel shows the scale in arcseconds. MNRAS **000**, 1–12 ()

**Figure 7.** (Continued).

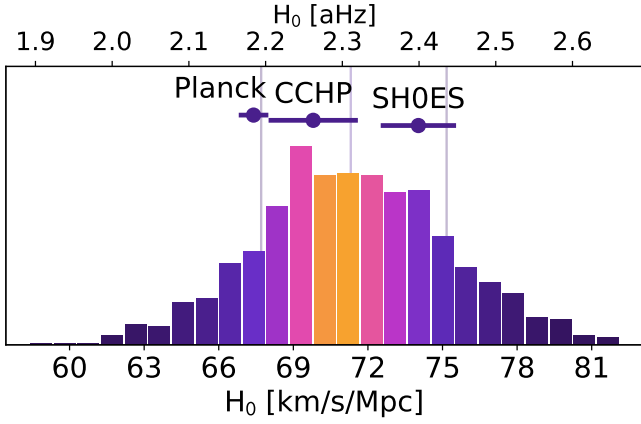


Figure 8. Histogram of the entire ensemble’s H_0 values. The ensemble consists of 8 simultaneously modelled quad systems. The vertical lines indicate 16th, 50th, and 84th percentiles of the distribution. To make the median furthermore easily discernible, the colouring of the histogram’s bars corresponds to the cumulative probability centred around the median (yellow-magenta-blue-black goes from 1 to 0). Horizontal error bars indicate recent measurements from other methods for comparison: Planck (Aghanim et al. 2018), CCHP (the Carnegie-Chicago Hubble Program; Freedman et al. 2019), and SHOES (the Supernovae H_0 for the Equation of State; Riess et al. 2019)

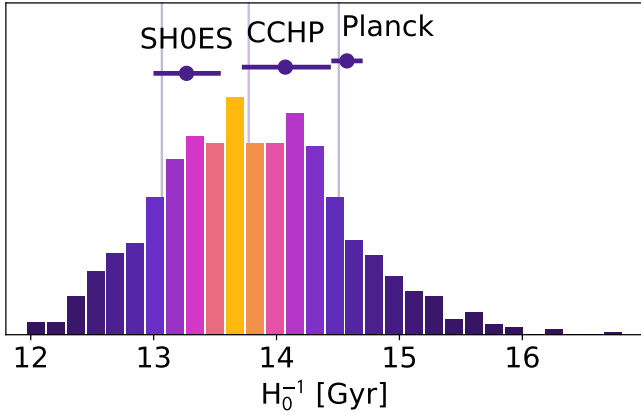


Figure 9. Histogram of the entire ensemble’s H_0^{-1} values, corresponding to the distribution in Figure 8.

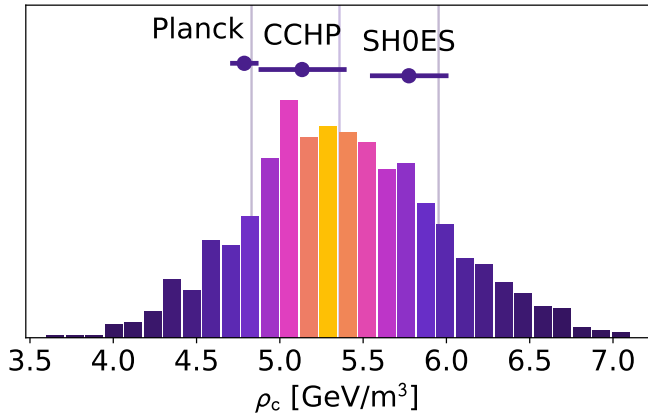


Figure 10. Histogram of the entire ensemble’s H_0^2 values in form of the cosmological critical density $\rho_c = 3/(8\pi G)H_0^2 c^2/e$ in GeV/m^3 , following Figure 8 and 9. It corresponds to an energy density of roughly 1 or 2 alpha particles per cubic metre.

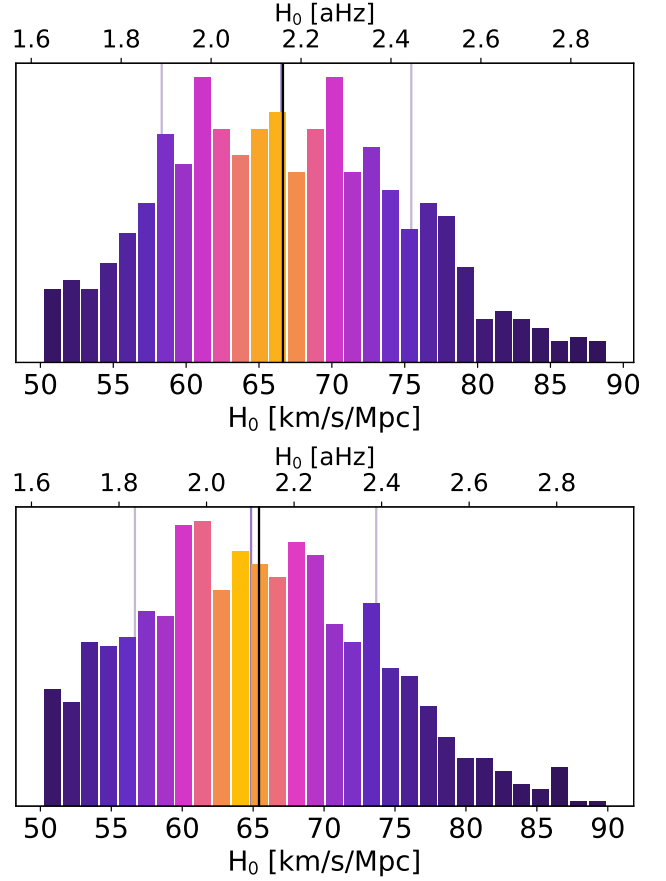


Figure 11. Best results for rung2 (top) and rung3 (bottom) of the TDLMC. Generally, we obtained best results from ensembles containing only quads which were simultaneously modelled. The ensembles each consist of 4 quad systems from the corresponding rung of the challenge. For these models an additional prior was used which required H_0 to be higher than 50 and lower than $90 \text{ km s}^{-1} \text{ Mpc}^{-1}$. Red vertical lines indicate the median 68 percent confidence range of $H_0 = 66.5^{+8.9}_{-8.2} \text{ km s}^{-1} \text{ Mpc}^{-1}$ for rung2 and $H_0 = 64.9^{+8.8}_{-8.2} \text{ km s}^{-1} \text{ Mpc}^{-1}$ for rung3. To make the median furthermore easily discernible, the colouring of the histogram bars corresponds to the cumulative probability centred around the median (yellow-magenta-blue-black goes from 1 to 0). The black vertical lines indicate the truth value for H_0 of the corresponding TDLMC rung. Note that these were the *best* results of each rung. The final submission also included models further from the truth, especially when they included doubles.